

A system for measuring auto- and cross-correlation of current noise at low temperatures

L. DiCarlo*, Y. Zhang*, D. T. McClure*, C. M. Marcus

Department of Physics, Harvard University, Cambridge, Massachusetts 02138, USA

L. N. Pfeiffer, K. W. West

Bell Laboratories, Lucent Technologies, Murray Hill, NJ 07974, USA

(Dated: November 5, 2018)

We describe the construction and operation of a two-channel noise detection system for measuring power and cross spectral densities of current fluctuations near 2 MHz in electronic devices at low temperatures. The system employs cryogenic amplification and fast-Fourier-transform based spectral measurement. The gain and electron temperature are calibrated using Johnson noise thermometry. Full shot noise of 100 pA can be resolved with an integration time of 10 s. We report a demonstration measurement of bias-dependent current noise in a gate defined GaAs/AlGaAs quantum point contact.

Over the last decade, measurement of electronic noise in mesoscopic conductors has successfully probed quantum statistics, chaotic scattering and many-body effects^{1,2}. Suppression of shot noise below the Poissonian limit has been observed in a wide range of devices, including quantum point contacts^{3,4,5}, diffusive wires^{6,7}, and quantum dots⁸, with good agreement between experiment and theory. Shot noise has been used to measure quasiparticle charge in strongly correlated systems, including the fractional quantum hall regime^{9,10} and normal-superconductor interfaces¹¹, and to investigate regimes where Coulomb interactions are strong, including coupled localized states in mesoscopic tunnel junctions¹² and quantum dots in the sequential tunneling¹³ and cotunneling¹⁴ regimes. Two-particle interference not evident in dc transport has been investigated using noise in an electronic beam splitter⁵.

Recent theoretical work^{15,16,17,18} proposes the detection of electron entanglement via violations of Bell-type inequalities using cross-correlations of current noise between different leads. Most noise measurements have investigated either noise auto-correlation^{3,5,6,9,14,19,20} or cross-correlation of noise in a common current^{4,7,8,12,21,22}, with only a few experiments^{23,24,25} investigating cross-correlation between two distinct currents. Henny *et al.*²³ and Oberholzer *et al.*²⁴ measured noise cross-correlation in the acoustic frequency range (low kHz) using room temperature amplification and a commercial fast Fourier transform (FFT)-based spectrum analyzer. Oliver *et al.*²⁵ measured cross-correlation in the low MHz using cryogenic amplifiers and analog power detection with hybrid mixers and envelope detectors.

In this paper, we describe a two-channel noise detection system for simultaneously measuring power spectral densities and cross spectral density of current fluctuations in electronic devices at low temperatures. Our ap-

proach combines elements of the two methods described above: cryogenic amplification at low MHz frequencies and FFT-based spectral measurement.

Several factors make low-MHz frequencies a practical range for low-temperature current noise measurement. This frequency range is high compared to the $1/f$ noise corner in typical mesoscopic devices. Yet, it is low enough that FFT-based spectral measurement can be performed efficiently with a personal computer (PC) equipped with a commercial digitizer. Key features of this FFT-based spectral measurement are near real-time operation and sufficient frequency resolution to detect spectral features of interest. Specifically, the fine frequency resolution provides information about the measurement circuit and amplifier noise at MHz, and enables extraneous interference pick-up to be identified and eliminated. These two features constitute a significant advantage over both wide-band analog detection of total noise power, which sacrifices resolution for speed, and swept-sine measurement, which sacrifices speed for resolution.

The paper is divided as follows. A block diagram of the system is presented in Section I. The amplification circuit is discussed in Section II. Section III describes the data analysis procedure, including digitization and FFT processing. A demonstration measurement of current noise in a quantum point contact (QPC) is presented in Section IV. System performance is discussed in Section V.

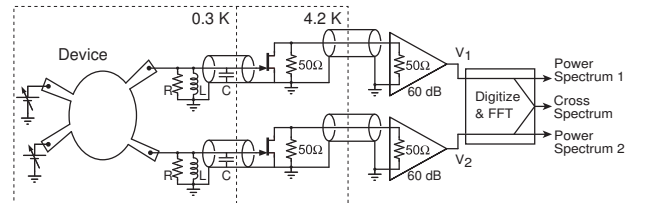


FIG. 1: Block diagram of the two-channel noise detection system, configured to measure the power spectral densities and cross spectral density of current fluctuations in a multi-terminal electronic device.

*These authors contributed equally to this work.

I. OVERVIEW OF THE SYSTEM

Figure 1 shows a block diagram of the two-channel noise detection system, which is integrated with a commercial ^3He cryostat (Oxford Instruments Heliox 2^{VL}). The system takes two input currents and amplifies their fluctuations in several stages. First, a parallel resistor-inductor-capacitor (RLC) circuit performs current-to-voltage conversion at frequencies close to its resonance at $f_o = (2\pi\sqrt{LC})^{-1} \approx 2$ MHz. Through its transconductance, a high electron mobility transistor (HEMT) operating at 4.2 K converts these voltage fluctuations into current fluctuations in a 50 Ω coaxial line extending from 4.2 K to room temperature. A 50 Ω amplifier with 60 dB of gain completes the amplification chain. The resulting signals V_1 and V_2 are simultaneously sampled at 10 MS/s by a two-channel digitizer (National Instruments PCI-5122) in a 3.4 GHz PC (Dell Optiplex GX280). The computer takes the FFT of each signal and computes the power spectral density of each channel and the cross spectral density.

II. AMPLIFIER

A. Design objectives

A number of objectives have guided the design of the amplification lines. These include:

1. Low amplifier input-referred voltage noise and current noise.
2. Simultaneous measurement of both noise at MHz and transport near dc.
3. Low thermal load.
4. Small size, allowing two amplification lines within the 52 mm bore cryostat.
5. Maximum use of commercial components.
6. Compatibility with high magnetic fields.

B. Overview of Circuit

Each amplification line consists of four circuit boards interconnected by coaxial cable, as shown in the circuit schematic in Fig. 2(a). Three of the boards are located inside the ^3He cryostat. The resonant circuit board (labeled RES in Fig. 2(a)) is mounted on the sample holder at the end of the 30 cm long coldfinger that extends from the ^3He pot to the center of the superconducting solenoid. The heat-sink board (SINK) anchored to the ^3He pot is a meandering line that thermalizes the inner conductor of the coaxial cable. The CRYOAMP board at the 4.2 K plate contains the only active element operating cryogenically, an Agilent ATF-34143 HEMT. The

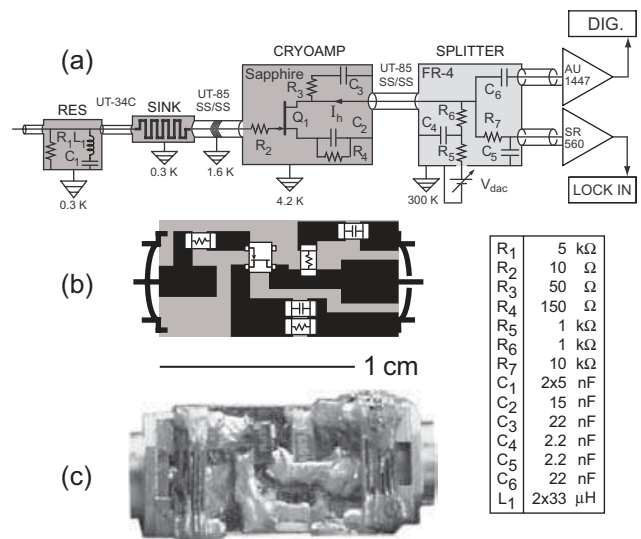


FIG. 2: (a) Schematic diagram of each amplification line. Values of all passive components are listed in the accompanying table. Transistor Q_1 is an Agilent ATF-34143 HEMT. (b) Layout of the CRYOAMP circuit board. Metal (black regions) is patterned by etching of thermally evaporated Cr/Au on sapphire substrate. (c) Photograph of a CRYOAMP board. The scale bar applies to both (b) and (c).

four-way SPLITTER board operating at room temperature separates low and high frequency signals and biases the HEMT. Each line amplifies in two frequency ranges, a low-frequency range below ~ 3 kHz and a high-frequency range around 2 MHz.

The low-frequency equivalent circuit is shown in Fig. 3(a): A resistor ($R_1 = 5$ k Ω) to ground, shunted by a capacitor ($C_1 = 10$ nF), converts an input current i to a voltage on the HEMT gate. The HEMT amplifies this gate voltage by ~ -5 V/V on its drain, which connects to a room temperature voltage amplifier at the low frequency port of the SPLITTER board. The low-frequency voltage amplifier (Stanford Research Systems model SR560) is operated in single-ended mode with ac coupling, 100 V/V gain and bandpass filtering (30 Hz to 10 kHz). The bandwidth in this low-frequency regime is set by the input time constant.

The high-frequency equivalent circuit is shown in Fig. 3(b). The inductor $L_1 = 66$ μH dominates over C_1 and forms a parallel RLC tank with R_1 and the capacitance $C \sim 96$ pF of the coaxial line connecting to the CRYOAMP board. Resistor R_4 is shunted by C_2 to enhance the transconductance at the CRYOAMP board. The coaxial line extending from 4.2 K to room temperature is terminated on both sides by 50 Ω . At room temperature, the signal passes through the high-frequency port of the SPLITTER board to a 50 Ω amplifier (MITEQ AU-1447) with a gain of 60 dB and a noise temperature of 100 K in the range 0.01 – 200 MHz.

C. Operating point

The HEMT must be biased in saturation to provide voltage (transconductance) gain in the low (high) frequency range. R_4 , $R_5 + R_6$ and supply voltage V_{dac} determine the HEMT operating point (R_1 grounds the HEMT gate at dc). A notable difference in this design compared to similar published ones regards the placement of R_4 . In previous implementations of similar circuits^{26,27,28}, R_4 is a variable resistor placed outside the refrigerator and connected to the source lead of Q_1 via a second coaxial line or low-frequency wire. Here, R_4 is located on the CRYOAMP board to simplify assembly and save space, at the expense of having full control of the bias point in Q_1 (R_4 fixes the saturation value of the HEMT current I_h). Using the I-V curves in Ref. 28 for a cryogenically cooled ATF-34143, we choose $R_4 = 150 \Omega$ to give a saturation current of a few mA. This value of saturation current reflects a compromise between noise performance and power dissipation. As shown in Fig. 4, Q_1 is biased by varying the supply voltage V_{dac} fed at the SPLITTER board. At the bias point indicated by a cross, the total power dissipation in the HEMT board is $I_h V_{h,ds} + I_h^2 R_4 = 1.8 \text{ mW}$, and the input-referred voltage noise of the HEMT is $\sim 0.4 \text{ nV}/\sqrt{\text{Hz}}$.

D. Passive Components

Passive components were selected based on temperature stability, size and magnetic field compatibility. All resistors (Vishay TNPW thin film) are 0805-size surface mount. Their variation in resistance between room temperature and 300 mK is $< 0.5\%$. Inductor L_1 (two 33 μH Coilcraft 1812CS ceramic chip inductors in series) does not have a magnetic core and is suited for operation at high magnetic fields. The dc resistance of L_1 is 26(0.3) Ω at 300(4.2) K. With the exception of C_1 , all capacitors are 0805-size surface mount (Murata COG GRM21). C_1 (two 5 nF American Technical Ceramics 700B NPO capacitors in parallel) is certified non-magnetic.

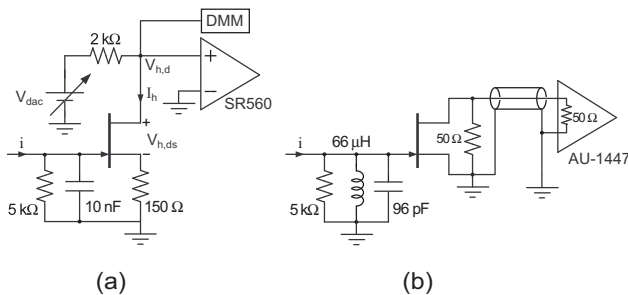


FIG. 3: Equivalent effective circuits characterizing the amplification line in the (a) low-frequency regime (up to $\sim 3 \text{ kHz}$), where it is used for differential conductance measurements, and in the (b) high-frequency regime (few MHz), where it is used for noise measurement.

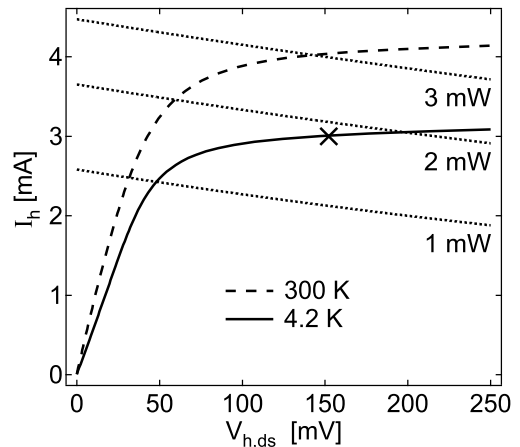


FIG. 4: Drain current I_h as a function of HEMT drain-source voltage $V_{h,ds}$, with the HEMT board at temperatures of 300 K (dashed) and 4.2 K (solid). These curves were obtained by sweeping the supply voltage V_{dac} and measuring drain voltage $V_{h,d}$ with an HP34401A digital multimeter (see Fig. 3(a)). From $V_{h,d}$ and V_{dac} , I_h and $V_{h,ds}$ were then extracted. Dotted curves are contours of constant power dissipation in the HEMT board. The HEMT is biased in saturation (cross).

E. Thermalization

To achieve a low device electron temperature, circuit board substrates must handle the heat load from the coaxial line. The CRYOAMP board must also handle the power dissipated by the HEMT and R_4 . Sapphire, having good thermal conductivity at low temperatures²⁹ and excellent electrical insulation, is used for the substrate in the RES, SINK and CRYOAMP boards. Polished blanks, 0.02" thick and 0.25" wide, were cut to lengths of 0.6" (RES and CRYOAMP) or 0.8" (SINK) using a diamond saw. Both planar surfaces were metallized with thermally evaporated Cr/Au (30/300 nm). Circuit traces were then defined on one surface using a Pulsar toner transfer mask and wet etching with Au and Cr etchants (Transene types TFA and 1020). Surface mount components were directly soldered.

The RES board is thermally anchored to the sample holder with silver epoxy (Epoxy Technology 410E). The CRYOAMP (SINK) board is thermalized to the 4.2 K plate (^3He pot) by a copper braid soldered to the back plane.

Semirigid stainless steel coaxial cable (Uniform Tube UT-85 SS-SS) is used between the SINK and CRYOAMP boards, and between the CRYOAMP board and room temperature. Between the RES and SINK boards, smaller coaxial cable (Uniform Tube UT-34 C) is used to conserve space.

With this approach to thermalization, the base temperature of the ^3He refrigerator is 290 mK with a hold time of $\sim 45 \text{ h}$. As demonstrated in Section IV, the electron base temperature in the device is also 290 mK.

III. DIGITIZATION AND FFT PROCESSING

The amplifier outputs V_1 and V_2 (see Fig. 1) are sampled simultaneously using a commercial digitizer (National Instruments PCI-5122) with 14-bit resolution at a rate $f_s = 10$ MS/s. To avoid aliasing³⁰ from the broadband amplifier background, V_1 and V_2 are frequency limited to below the Nyquist frequency of 5 MHz using 5-pole Chebyshev low-pass filters, built in-house from axial inductors and capacitors with values specified by the design recipe in Ref. 31. The filters have a measured half power frequency of 3.8 MHz, 39 dB suppression at 8 MHz and a pass-band ripple of 0.03 dB.

While the digitizer continuously stores acquired data into its memory buffer (16 MB per channel), a software program processes the data from the buffer in blocks of $M = 10,368$ points per channel. M is chosen to yield a resolution bandwidth $f_s/M \sim 1$ kHz, and to be factorizable into powers of two and three to maximize the efficiency of the FFT algorithm.

Each block of data is processed as follows. First, V_1 and V_2 are multiplied by a Hanning window $W_H[m] = \sqrt{2/3}(1 - \cos(2\pi m/M))$ to avoid end effects³⁰. Second, using the FFTW package³², their FFTs are calculated:

$$\tilde{V}_{1(2)}[f_n] = \sum_{m=0}^{M-1} W_H[m] V_{1(2)}(t_m) e^{-i2\pi f_n t_m},$$

where $t_m = m/f_s$, $f_n = (n/M)f_s$, and $n = 0, 1, \dots, M/2$. Third, the power spectral densities $P_{1,2} = 2|\tilde{V}_{1,2}|^2/(Mf_s)$ and the cross spectral density $X = 2(\tilde{V}_1^* \cdot \tilde{V}_2)/(Mf_s) = X_R + iX_I$ are computed.

As blocks are processed, running averages of P_1 , P_2 , and X are computed until the desired integration time τ_{int} is reached. With the 3.4 GHz computer and the FFTW algorithm, these computations are carried out in nearly real-time: it takes 10.8 s to acquire and process 10 s of data.

IV. MEASUREMENT: QPC CURRENT NOISE

In this section, the system is demonstrated with measurements of current noise in a quantum point contact (QPC). Specifically, the partition noise S_I^P is measured as a function of QPC source-drain bias V_{sd} :

$$S_I^P(V_{\text{sd}}) = S_I(V_{\text{sd}}) - 4k_B T_e g(V_{\text{sd}}). \quad (1)$$

Here, S_I is the total QPC current noise spectral density without extraneous noise (1/f, random telegraph, pick-up), k_B is the Boltzmann constant, T_e is the electron temperature, $g(V_{\text{sd}}) = dI/dV_{\text{sd}}$ is the bias-dependent QPC differential conductance, and I is the current through the QPC.

A. Device and Setup

The QPC is defined by two electrostatic gates on the surface of a GaAs/Al_{0.3}Ga_{0.7}As heterostructure grown by molecular beam epitaxy. The two-dimensional electron gas (2DEG) 190 nm below the surface has a density $1.7 \times 10^{11} \text{ cm}^{-2}$ and mobility $5.6 \times 10^6 \text{ cm}^2/\text{Vs}$. The QPC conductance is controlled by negative voltages V_{g1} and V_{g2} applied to the electrostatic gates.

The QPC is connected to the system as shown in the inset of Fig. 5. The two amplification lines are connected to the same reservoir of the QPC. In this case, the two input RLC tanks effectively become a single tank with resistance $R' \approx 2.5 \text{ k}\Omega$, inductance $L' \approx 33 \text{ }\mu\text{H}$ and capacitance $C' \approx 192 \text{ pF}$. The QPC current noise couples to both amplification lines and thus can be extracted from either the single channel power spectral densities or the cross spectral density. The latter has the technical advantage of rejecting any noise not common to both amplification lines. It is used to extract S_I^P in the remainder of this section.

A $25 \text{ }\mu\text{V}_{\text{rms}}$, 430 Hz excitation V_{ac} is applied to the other QPC reservoir and used for lock-in measurement of g . A dc bias voltage V_{dc} is also applied to generate a finite V_{sd} . V_{sd} deviates from V_{dc} due to the resistance in-line with the QPC, which is equal to the sum of $R_1/2$ and ohmic contact resistance R_s . V_{sd} could in principle be measured by the traditional four-wire technique. This would require additional low-frequency wiring, as well as filtering to prevent extraneous pick-up and room-temperature amplifier noise from coupling to the noise measurement circuit. For technical simplicity, here V_{sd} is obtained by numerical integration of the measured bias-dependent g :

$$V_{\text{sd}} = \int_0^{V_{\text{dc}}} \frac{dV}{1 + (R_1/2 + R_s)g(V)} \quad (2)$$

B. Measurement

Figure 5 shows linear conductance $g(V_{\text{sd}} = 0)$ as a function of V_{g2} , at a fridge temperature $T_{\text{fridge}} = 290 \text{ mK}$ (base temperature). Here, g was extracted from lock-in measurements using amplification line 1. As neither the low frequency gain of amplifier 1 nor R_s were known precisely beforehand, these parameters were calibrated by aligning the observed conductance plateaus to the expected multiples of $2e^2/h$. This method yielded a low frequency gain -4.6 V/V and $R_s = 430 \text{ }\Omega$.

Figure 6 shows P_1 , P_2 , X_R , and X_I as a function of frequency f , at base temperature and with the QPC pinched off ($g = 0$). $P_{1(2)}$ shows a peak at the resonant frequency of the RLC tank, on top of a background of approximately $85(78) \times 10^{-15} \text{ V}^2/\text{Hz}$. The background in $P_{1(2)}$ is due to the voltage noise $S_{V,1(2)}$ of amplification line 1(2) ($\sim 0.4 \text{ nV}/\sqrt{\text{Hz}}$). The peak results from thermal noise of the resonator resistance and current noise ($S_{I,1} + S_{I,2}$)

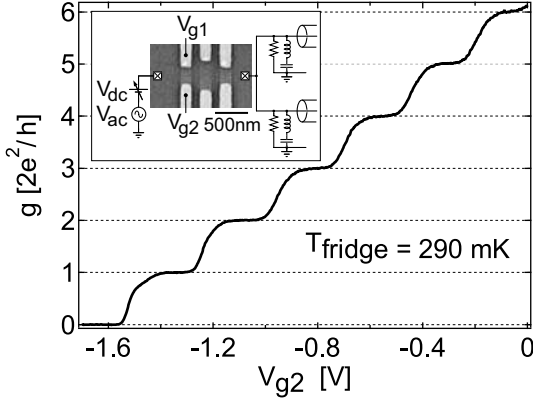


FIG. 5: Inset: Setup for detection of QPC current noise and electron micrograph of a device identical in design to the one used. The QPC is defined by negative voltages V_{g1} and V_{g2} applied on two facing gates. All other gates in the device are grounded. Main: linear conductance $g(V_{sd} = 0)$ as a function of V_{g2} at 290 mK, measured using amplification line 1. $V_{g1} = -3.2$ V.

from the amplifiers. X_R picks out this peak and rejects the amplifier voltage noise backgrounds. The inset zooms in on X_R near the resonant frequency. The solid curve is a best-fit to the form

$$X_R(f) = \frac{X_R^0}{1 + (f^2 - f_o^2)^2 / (f \Delta f_{3dB})^2}, \quad (3)$$

corresponding to the lineshape of white noise band-pass filtered by the RLC tank. The fit parameters are the peak height X_R^0 , the half-power bandwidth Δf_{3dB} and the peak frequency f_o . Power spectral densities $P_{1(2)}$ can be fit to a similar form including a fitted background

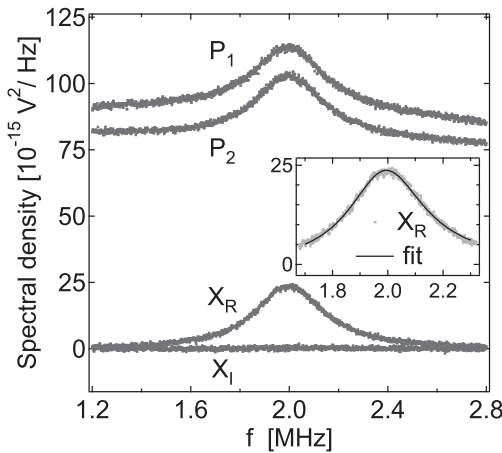


FIG. 6: Power spectral densities P_1 and P_2 , and real and imaginary parts X_R and X_I of the cross spectral density, at base temperature and with the QPC pinched off ($g = 0$), obtained from noise data acquired for $\tau_{int} = 20$ s. Inset: expanded view of X_R near resonance, along with a fit using Eq. (3) over the range 1.7 to 2.3 MHz.

term:

$$P_{1(2)}(f) = P_{1(2)}^B + \frac{P_{1(2)}^0}{1 + (f^2 - f_o^2)^2 / (f \Delta f_{3dB})^2}, \quad (4)$$

C. Noise measurement calibration

In order to extract S_I^P from $X_R(f)$, the noise measurement system must be calibrated *in situ*. An effective circuit with noise sources is defined for this purpose and shown in Fig. 7. Within this circuit model, S_I^P is given by:

$$S_I^P = \left(\frac{X_R^0}{G_X^2} - 4k_B T_e R_{eff} \right) \left(\frac{1 + g R_s}{R_{eff}} \right)^2 \quad (5)$$

Here, $G_X = \sqrt{G_1 G_2}$ is the cross-correlation gain and $R_{eff} = 2\pi f_o^2 L' / \Delta f_{3dB}$ is the total effective resistance parallel to the tank³³.

Calibration requires assigning values for R_s , T_e , and G_X . While the value $R_s = 430 \Omega$ is known from the conductance measurement, G_X and T_e are calibrated from thermal noise measurements. The procedure demonstrated in Fig. 8 stems from the relation $X_R^0 = 4k_B T_e R_{eff} G_X^2$ ³⁴ valid at $V_{sd} = 0$.

First, $X_R(f)$ is measured over $\tau_{int} = 30$ s for various V_{g2} settings at each of three elevated fridge temperatures ($T_{fridge} = 3.1, 4.2,$ and 5.3 K). X_R^0 and R_{eff} are extracted from fits to $X_R(f)$ using Eq. (3) and plotted parametrically (open markers in Fig. 8(a)). A linear fit (constrained to pass through the origin) to each parametric plot gives the slope dX_R^0/dR_{eff} at each temperature, equal to $4k_B T_e G_X^2$. Assuming $T_e = T_{fridge}$ at these temperatures, $G_X = 790$ V/V is extracted from a linear fit to $dX_R^0/dR_{eff}(T_{fridge})$, shown in Fig. 8(b).

Next, the base electron temperature is calibrated from a parametric plot of X_R^0 as a function of R_{eff} obtained from similar measurements at base temperature (solid circles in Fig. 8(a)). From the fitted slope dX_R^0/dR_{eff} (black marker in Fig. 8(b)) and using the calibrated G_X , a value $T_e = 290$ mK is obtained. This suggests that electrons are well thermalized to the fridge.

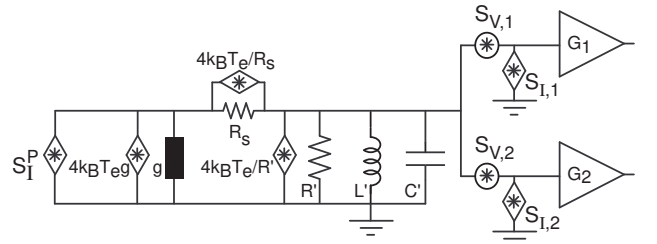


FIG. 7: Circuit model used for extraction of the QPC partition noise S_I^P . $G_{1(2)}$ is the voltage gain of amplification line 1(2) between HEMT gate and digitizer input.

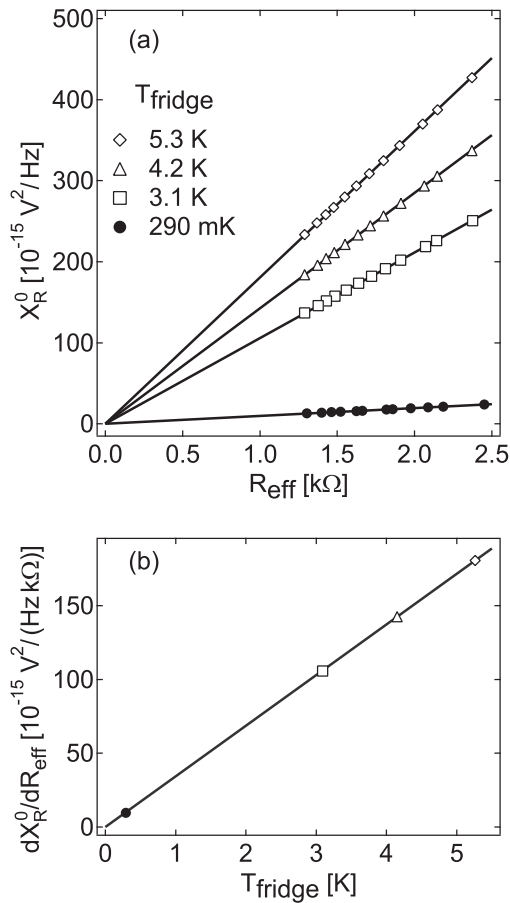


FIG. 8: Calibration by noise thermometry of the electron temperature T_e at base fridge temperature and the cross-correlation gain G_X . (a) X_R^0 as function of R_{eff} (both from fits to $X_R(f)$ using Eq. (3)), at base (solid circles) and at three elevated fridge temperatures (open markers). Solid lines are linear fits constrained to the origin. (b) Slope dX_R^0/dR_{eff} (from fits in (a)) as a function of T_{fridge} . Solid line is a linear fit (constrained to the origin) of dX_R^0/dR_{eff} at the three elevated temperatures (open markers).

D. QPC partition noise

Following the calibration, $S_I^P(V_{\text{sd}})$ is extracted as follows. $X_R(f)$ and g are simultaneously measured ($\tau_{\text{int}} = 60$ s) at fixed V_{g2} as a function of V_{sd} between -150 μV and $+150$ μV . At each V_{sd} setting, X_R^0 and R_{eff} are obtained from fits of $X_R(f)$ to Eq. (3), and used with the measured g to extract $S_I^P(V_{\text{sd}})$ from Eq. (5).

Demonstration measurements of $S_I^P(V_{\text{sd}})$ are shown in Fig. 9. Open markers superimposed on the linear conductance trace in Fig. 9(a) indicate V_{g2} settings giving $g(V_{\text{sd}} = 0) \approx 0, 0.5, 1, 1.5,$ and $2 \times 2e^2/h$. The corresponding noise data are shown in Fig. 9(b). At 0, 1 and $2 \times 2e^2/h$, where the QPC is either pinched off or on a linear conductance plateau, S_I^P shows little dependence on bias, in contrast with the $|V_{\text{sd}}|$ dependence observed when $g \approx 0.5$ and $1.5 \times 2e^2/h$. This behavior is consistent with earlier experiments^{3,4} and theory^{35,36} of shot noise

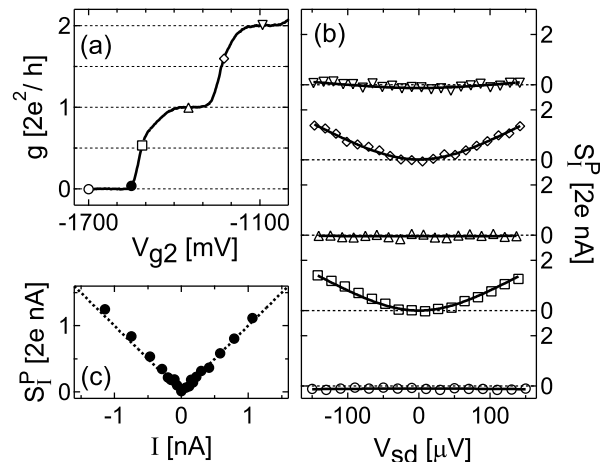


FIG. 9: (a) Linear conductance $g(V_{\text{sd}} = 0)$ as a function of V_{g2} . Open and solid markers indicate V_{g2} settings for the noise measurements shown in (b) and (c), respectively. (b) QPC partition noise S_I^P as a function of V_{sd} , for conductances near 0, 0.5, 1, 1.5, and $2 \times 2e^2/h$. Solid lines are fits to Eq. (6) using \mathcal{N} as the only fitting parameter. (c) S_I^P as a function of dc current I with the QPC near pinch-off. The dotted line represents full shot noise $S_I^P = 2e|I|$.

in a QPC.

Within mesoscopic scattering theory^{1,2}, where transport is described by transmission coefficients $\tau_{n,\sigma}$ (n is the sub-band index and σ denotes spin), S_I^P is given by

$$S_I^P(V_{\text{sd}}) = 2 \frac{2e^2}{h} \mathcal{N} \left[eV_{\text{sd}} \coth \left(\frac{eV_{\text{sd}}}{2k_B T_e} \right) - 2k_B T_e \right], \quad (6)$$

with a *noise factor* $\mathcal{N} = \frac{1}{2} \sum \tau_{n,\sigma} (1 - \tau_{n,\sigma})$. This equation is strictly valid for constant transmission coefficients across the bias window. At low-temperatures and for the spin-degenerate case, \mathcal{N} is zero at multiples of $2e^2/h$ and reaches a maximum value of 0.25 at odd multiples of $0.5 \times 2e^2/h$. Fits to the $S_I^P(V_{\text{sd}})$ data in Fig. 9(b) using the form of Eq. (6) are shown as solid curves, with $T_e = 290$ mK and best-fit \mathcal{N} values of 0.00, 0.20, 0.00, 0.19, and 0.03 for $g \approx 0, 0.5, 1, 1.5,$ and $2 \times 2e^2/h$, respectively. The deviation of the best-fit \mathcal{N} from 0.25 near 0.5 and $1.5 \times 2e^2/h$ is discussed in detail in Ref. 37.

A measurement of S_I^P as a function of I with the QPC barely open (solid marker in Fig. 9(a)) is shown in Fig. 9(c). In this regime, full shot noise $S_I^P = 2e|I|$ is observed. This is consistent with scattering theory and with recent measurements on mesoscopic tunnel barriers free of impurities, localized states and $1/f$ noise³⁸.

V. SYSTEM PERFORMANCE

The resolution in the estimation of current noise spectral density from one-channel and two-channel measurements is determined experimentally in this final section. Noise data are first sampled over a total time $\tau_{\text{tot}} = 1$ h,

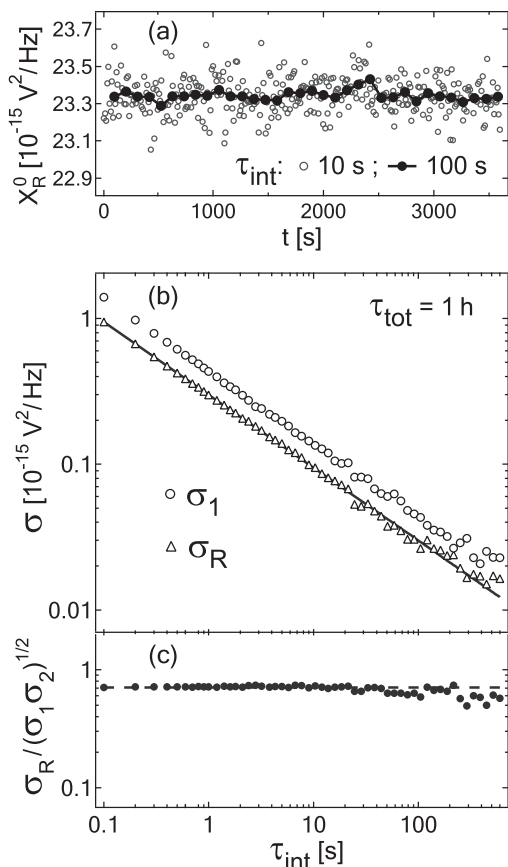


FIG. 10: (a) X_R^0 as a function of time t , for τ_{int} of 10 s (open circles) and 100 s (solid circles). (b) Standard deviations σ_1 and σ_R as a function of τ_{int} . Solid line is a fit to σ_R of the form $C \cdot \tau_{\text{int}}^{-1/2}$, with best-fit value $C = 0.30 \times 10^{-15} \text{ s}^{1/2} \text{V}^2/\text{Hz}$. (c) $\sigma_R / \sqrt{\sigma_1 \sigma_2}$ as a function of τ_{int} . The dashed line is a constant $1/\sqrt{2}$.

with the QPC at base temperature and pinched off. Dividing the data in segments of time length τ_{int} , calculating the power and cross spectral densities for each segment, and fitting with Eqs. (3) and (4) gives a sequence of $\tau_{\text{tot}}/\tau_{\text{int}}$ peak heights for each of P_1 , P_2 and X_R . Shown in open (solid) circles in Fig. 10(a) is X_R^0 as a function of time t for $\tau_{\text{int}} = 10(100)$ s. The standard deviation σ_R of X_R^0 is $1(0.3) \times 10^{-16} \text{ V}^2/\text{Hz}$. The resolution δS_I in current noise spectral density is given by $\sigma_R / (G_X^2 R_{\text{eff}}^2)$ (see Eq. (5)). For $\tau_{\text{int}} = 10$ s, $\delta S_I = 2.8 \times 10^{-29} \text{ A}^2/\text{Hz}$, which corresponds to full shot noise $2eI$ of $I \sim 100$ pA.

The effect of integration time on the resolution is determined by repeating the analysis for different values of τ_{int} . Fig. 10(b) shows the standard deviation σ_1 (σ_R) of P_1^0 (X_R^0) as a function of τ_{int} . The standard deviation σ_2 of P_2^0 , not shown, overlaps closely with σ_1 . All three standard deviations scale as $1/\sqrt{\tau_{\text{int}}}$, consistent with the

Dicke radiometer formula³⁹ which applies when measurement error results only from finite integration time, i.e., it is purely statistical. This suggests that, even for the longest segment length of $\tau_{\text{int}} = 10$ min, the measurement error is dominated by statistical error and not by instrumentation drift on the scale of 1 h.

Figure 10(c) shows $\sigma_R / \sqrt{\sigma_1 \sigma_2}$ as a function of τ_{int} . This ratio gives the fraction by which, in the present measurement configuration, the statistical error in current noise spectral density estimation from X_R^0 is lower than the error in the estimation from either P_1^0 or P_2^0 alone. The geometric mean in the denominator accounts for any small mismatch in the gains G_1 and G_2 . In theory, and in the absence of drift, this ratio is independent of τ_{int} and equal to $1/\sqrt{2}$ when the uncorrelated amplifier voltage noise ($S_{V,1(2)}$) dominates over the noise common to both amplification lines. The ratio would be unity when the correlated noise dominates over $S_{V,1(2)}$.

The experimental $\sigma_R / \sqrt{\sigma_1 \sigma_2}$ is close to $1/\sqrt{2}$ (dashed line). This is consistent with the spectral density data in Fig. 6, which shows that the backgrounds in P_1 and P_2 are approximately three times larger than the cross-correlation peak height. The ratio deviates slightly below $1/\sqrt{2}$ at the largest τ_{int} values. This may result from enhanced sensitivity to error in the subtraction of the $P_{1(2)}$ background at the longest integration times.

A similar improvement relative to estimation from either P_1^0 or P_2^0 alone would also result from estimation with a weighted average $(P_1^0/G_1^2 + P_2^0/G_2^2)G_X^2/2$. The higher resolution attainable from two channel measurement relative to single-channel measurement in this regime has been previously exploited in noise measurements in the kHz range^{4,21,22}.

VI. CONCLUSION

We have presented a two-channel noise detection system measuring auto- and cross-correlation of current fluctuations near 2 MHz in electronic devices at low temperatures. The system has been implemented in a ^3He refrigerator where the base device electron temperature, measured by noise thermometry, is 290 mK. Similar integration with a ^3He - ^4He dilution refrigerator would enable noise measurement at temperatures of tens of mK.

We thank N. J. Craig, J. B. Miller, E. Onitskansky, and S. K. Slater for device fabrication. We also thank H.-A. Engel, D. C. Glatli, P. Horowitz, W. D. Oliver, D. J. Reilly, P. Roche, A. Yacoby, Y. Yamamoto for valuable discussion, and B. D'Urso, F. Molea and H. Steinberg for technical assistance. We acknowledge support from NSF-NSEC, ARDA/ARO, and Harvard University.

¹ Ya. M. Blanter and M. Büttiker, Phys. Rep. **336**, 1 (2000).
Ya. M. Blanter, cond-mat/0511478 (2005).

² T. Martin, in *Nanophysics: Coherence and Transport*, Les

- Houches Session LXXXI, edited by H. Bouchiat *et al.* (Elsevier, Amsterdam, 2005), cond-mat/0501208.
- ³ M. Reznikov *et al.*, Phys. Rev. Lett. **75**, 3340 (1995).
 - ⁴ A. Kumar *et al.*, Phys. Rev. Lett. **76**, 2778 (1996).
 - ⁵ R. C. Liu *et al.*, Nature **391**, 263 (1998).
 - ⁶ A. H. Steinbach *et al.*, Phys. Rev. Lett. **76**, 3806 (1996).
 - ⁷ M. Henny *et al.*, Phys. Rev. B **59**, 2871 (1999).
 - ⁸ S. Oberholzer *et al.*, Phys. Rev. Lett. **86**, 2114 (2001).
 - ⁹ R. de-Picciotto *et al.*, Nature **389**, 162 (1997). M. Reznikov *et al.*, Nature **399**, 238 (1999).
 - ¹⁰ L. Saminadayar *et al.*, Phys. Rev. Lett. **79**, 2526 (1997).
 - ¹¹ X. Jehl *et al.*, Nature **405**, 50 (2000).
 - ¹² S. S. Safonov *et al.*, Phys. Rev. Lett. **91**, 136801 (2003).
 - ¹³ S. Gustavsson *et al.*, Phys. Rev. Lett. **96**, 076605 (2006).
 - ¹⁴ E. Onac *et al.*, Phys. Rev. Lett. **96**, 026803 (2006).
 - ¹⁵ T. Martin, A. Crepieux and N. Chtchelkatchev, in *Quantum Noise in Mesoscopic Physics*, NATO Science Series II **97**, edited by Yu. V. Nazarov (Kluwer, Dordrecht, 2003), cond-mat/0209517.
 - ¹⁶ P. Samuelsson *et al.*, Phys. Rev. Lett. **92**, 026805 (2004).
 - ¹⁷ C. W. J. Beenakker *et al.*, in *Fundamental Problems in Mesoscopic Physics*, NATO Science Series II **154**, edited by I. V. Lerner, B. L. Altshuler and Y. Gefen (Kluwer, Dordrecht, 2004), cond-mat/0310199.
 - ¹⁸ A. V. Lebedev *et al.*, Phys. Rev. B **71**, 045306 (2005).
 - ¹⁹ R. J. Schoelkopf *et al.*, Phys. Rev. Lett. **78**, 3370 (1997).
 - ²⁰ L. A. Spietz *et al.*, Science **300**, 1929 (2003).
 - ²¹ D. C. Glattli *et al.*, J. Appl. Phys. **81**, 7350 (1997).
 - ²² M. Sampietro, L. Fasoli and G. Ferrari, Rev. Sci. Instrum. **70**, 2520 (1999). G. Ferrari and M. Sampietro, Rev. Sci. Instrum. **73**, 2717 (2002).
 - ²³ M. Henny *et al.*, Science **284**, 296 (1999). S. Oberholzer *et al.*, Physica E **6**, 314 (2000).
 - ²⁴ S. Oberholzer *et al.*, Phys. Rev. Lett. **96**, 046804 (2006).
 - ²⁵ William D. Oliver *et al.*, Science **284**, 299 (1999).
 - ²⁶ Adrian T. Lee, Rev. Sci. Instrum. **60**, 3315 (1989).
 - ²⁷ Adrian Tae-Jin Lee, Rev. Sci. Instrum. **64**, 2373 (1993).
 - ²⁸ A. M. Robinson and V. I. Talyanskii, Rev. Sci. Instrum. **75**, 3169 (2004).
 - ²⁹ F. Pobell, *Matter and Methods at Low Temperatures*, Second Edition, (Springer-Verlag, Berlin, 1996).
 - ³⁰ A. V. Oppenheim and R. W. Schaffer, *Discrete-Time Signal Processing*, (Prentice Hall, Englewood Cliffs, 1989).
 - ³¹ Jon B. Hagen, *Radio-Frequency Electronics*, (Cambridge University Press, Cambridge, 1996).
 - ³² M. Frigo and S. G. Johnson, Proceedings of the International Conference on Acoustics, Speech, and Signal Processing **3**, 1381 (1998).
 - ³³ Within the model (Fig. 7), $R_{\text{eff}} = (1/(1/g + R_s) + 1/R')^{-1}$. A measurement of $\Delta f_{3\text{dB}}$ with the QPC pinched off ($g = 0$) gives $R' = 2.4 \text{ k}\Omega$. This small reduction from $2.5 \text{ K}\Omega$ reflects small inductor and capacitor losses near the resonant frequency.
 - ³⁴ The full expression within the circuit model is $X_R^0 = (4k_B T_e R_{\text{eff}} + (S_{I,1} + S_{I,2}) R_{\text{eff}}^2) G_X^2$. The linear dependence of X_R^0 on R_{eff} observed in Fig. 8(a) demonstrates that the quadratic term from amplifier current noise is negligible.
 - ³⁵ G. B. Lesovik, Pis'ma Zh. Eksp. Teor. Fiz. **49**, 513 (1989). [JETP. Lett. **49**, 592 (1989)].
 - ³⁶ M. Büttiker, Phys. Rev. Lett. **65**, 2901 (1990).
 - ³⁷ L. DiCarlo *et al.*, cond-mat/0604019 (2006).
 - ³⁸ Y. Chen and R. A. Webb, Phys. Rev. B **73**, 035424 (2006).
 - ³⁹ R. H. Dicke, Rev. Sci. Instrum. **17**, 268 (1946).